AFM tip-based mechanical nanomachining of 3D micro and nano-structures via the control of the scratching trajectory

Yanquan Geng[1,2,3], Yongda Yan[1,2,*], Emmanuel Brousseau[3], Yanwen Sun[1,2]

[1] *The State Key Laboratory of Robotics and Systems, Robotics Institute, Harbin Institute of Technology, Harbin, Heilongjiang 150080, P.R. China*

[2] *Center for Precision Engineering, Harbin Institute of Technology, Harbin, Heilongjiang 150001, P.R. China*

[3] *Cardiff School of Engineering, Cardiff University, Cardiff, UK*

** Corresponding author. Tel.: +86-0451-86412924. Fax: +86-0451-86415244*

E-mail address: yanyongda@hit.edu.cn *(Y. D. Yan)*

Abstract

This paper presents a novel mechanical material removal method to produce nanostructures with a precise control of their three dimensional (3D) surface topography. The method employs the tip of an atomic force microscope (AFM) probe as the cutting tool and a closed-loop high precision stage to control the machining path of the tip. In this approach, the tip only describes vertical motions while the stage is actuated along lateral directions in a raster scan strategy. The machining of features with 3D nanoscale topography in this way is the combined result of the tip applying a constant normal load on the sample while varying the distance (i.e. the feed) between two parallel lines of cut. More specifically, an increased feed leads to a reduced machining depth and vice-versa. Thus, the main difference with mechanical milling or

turning at such small scale is that this method relies on the control of the feed to determine the machined depth. To support the interpretation of the process outcomes, an analytical model is developed. This model expresses the relationship between the feed and the machined depth as a function of the contact area between the tip and the material. The critical achievable slope of produced nanostructures was derived from this model and validated using experimental tests. This parameter corresponds to the maximum inclination of the surface of a nanostructure that can be machined with the proposed method. From the knowledge of the critical slope, the machining of periodic nanostructures was demonstrated on a single crystal copper workpiece. In principle, the method reported here could be implemented to any instrument with micro- and nano-indentation capabilities by exploiting their load-control feedback mechanism.

Keywords: Atomic force microscope, mechanical nanomachining, three dimensional micro and nano-structures, scratching trajectory.

1. Introduction

The recent and rapid development of nanotechnology-based functionalities incorporated in new devices has resulted in the increased need to develop processes for the fabrication of three-dimensional micro- and nanostructures (3D-MNS). These 3D-MNS find applications in various fields, such as in ultra-large scale integration (ULSI) circuits (Thompson and Parthasarathy, 2006), nanoelectromechanical systems (NEMS) (Lyshevski, 2002) and surface-enhanced Raman spectroscopy (SERS) substrates (Li et al., 2010). The fabrication of such structures brings new challenges to

manufacturing engineers. A number of methods exist to produce 3D-MNS. These include nanoimprint lithography (Yao et al., 2011), electrochemical machining (Zhan et al., 2016), and focused ion beam nanolithography (Xu et al., 2009). However, these are generally limited by their low throughput, complexity and/or cost of implementation. An alternative approach for the manufacturing of such structures relies on using the tip of an atomic force microscope (AFM) probe as a sub-micrometre fabrication tool. In particular, since the invention of the AFM in 1986 by Binnig et al., (1986), such an instrument has proved to be a powerful platform for nanofabrication. This is due to its achievable nanoscale accuracy, its ability to operate in an atmospheric environment and the large range of materials to which it can be applied (Tseng 2011). Numerous studies have been conducted to fabricate one dimensional (1D) and two dimensional (2D) nanostructures using an AFM tip-based nanofabrication technique (Garcia et al., 2014). More recently, increased attention has also been paid by researchers towards the machining of 3D-MNS using this approach. Pires et al. (2011) used thermochemical scanning probe lithography to achieve the 3D replica of a well-known mountain summit written into a glassy organic resist. The authors used a layer-by-layer approach for material removal. In the reported implementation 120 layers were needed to create the 3D structure over a 2 μm × 2 μm area. Chen et al. (2005) fabricated convex and concave lenses with diameters between 2 μm and 4 μm using the tip-based local anodic oxidation (LAO) technique on a Si substrate. To control the topography of these 3D features, the authors varied the oxidation voltage supplied by the tip according to a pre-defined gray-scale map of the

lenses. Guo et al. (2015) proposed an AFM tip-based tribochemistry-induced nanofabrication method to obtain multilayered nanostructures on a Si(100) surface. These studies indicate that the AFM tip-based fabrication method is suitable for the manufacture of 3D-MNS. However, the methods reported above may be restricted by their relative complexity, the limited set of processable materials, the need for subsequent processing, and/or the rigorous control of the operating environment.

Among the many AFM tip-based nanofabrication methods, the direct mechanical machining approach is the simplest and most flexible to implement. As a result, it has been intensively studied in recent years (Yan et al., 2015). To date, there are essentially only two strategies, which have been developed to fabricate 3D-MNS using this nano-scale material removal process, namely the layer-by-layer machining approach and the direct control of the normal load applied by the tip on the sample surface (Deng et al., 2016). For the layer-by-layer approach, Geng et al. (2013a) recently proposed to use a combination of the movement of a high precision stage and that of the AFM tip to fabricate nanochannels that exhibit a floor surface with different step heights. Based on this, a millimeter-long nanochannel with such nanostructures was achieved (Yan et al., 2014). However, the layer-by-layer approach generally leads to the formation of relatively large burrs and results in machined features that display a stepped topography on curved or inclined surfaces. For this reason, more attention has been paid to the normal load-control approach. Yan et al. (2010) first proposed such a method to achieve 3D-MNS. In this case, the gray-scale

information of the image of the features to produce was used to define the normal load applied by the tip on the sample surface. However, in this study, the machined depth of the machined 3D-MNS could not be accurately predicted. To solve this issue, Geng et al. (2013b) developed a theoretical model to calculate, a-priori, the normal load that should be applied to achieve a given depth. Based on this model, a sinusoidal waveform nanostructure with good quality was machined successfully. However, a drawback associated with this approach is that a very accurate synchronization is required between the relative vertical and lateral motions of the tip. In particular, given that each pixel in the gray-scale map of a nanostructure may correspond to a specific load, this results in a relatively time-consuming process to implement in practice. Due to the respective limitations of the studies reported above for the nanoscale machining of 3D-MNS, an alternative method was proposed recently by the authors. It relied on the frequency control of the tip lateral reciprocating motions along the fast axis of the raster scan (Geng et al., 2016a). In particular, the key characteristic of this method is that it enabled the variation of the feed during machining, which in turn, allowed the variation of the machined depth. Although this approach successfully demonstrated the fabrication of 3D-MNS on a single crystal copper substrate, it is restricted to the generation of triangular probe trajectories. This results in an inconsistent machined depth along the width of the produced 3D-MNS. Moreover, the authors noted that the acceleration and deceleration of the AFM tip in one machining cycle could cause inaccuracies when producing periodic 3D-MNS. Therefore, an optimized processing method is still

required for enhancing such a feed control-based approach.

For this reason, in the present study, a novel method is proposed to generate a more flexible control and a wider range of machining trajectories of the AFM tip while still implementing the feed control concept. In particular, this method relies on employing a high precision stage to define relative lateral displacements between the AFM tip and the sample in a flexible raster scan fashion while the AFM tip is actuated in the vertical direction only. More specifically, the control of the tip motions relies on the built-in feedback loop of the AFM instrument to ensure that a constant normal load is applied on the sample. In addition, the distance between two parallel machining lines, i.e the feed, can be controlled very accurately, which can guarantee the accuracy of the periodicity of the 3D-MNS. An analytical model was also developed to help interpreting the achieved topography of the machined features. This model defines the relationship between the feed and the achieved depth as a function of the contact area between the tip and the material. Based on this, the critical achievable slope of the 3D-MNS could be derived. This value was then further refined using experimental tests. In addition the minimum period of such 3D-MNS was obtained. Finally, the successful fabrication of several typical periodic 3D-MNS was demonstrated.

2. Experiments

2.1 Experimental setup

Fig. 1 (a) shows the schematic of the modified AFM-based nanomachining system utilised. It includes a commercial AFM instrument (Dimension 3100, Veeco Inc., USA) and a closed-loop high precision stage (P517-3CD, PI Company, Germany). The high precision stage was employed to achieve the planned trajectories because the resolution of the original stage of the AFM instrument was too low and thus, could not meet the experimental requirements. The high precision stage was fixed on the coarse stage of the AFM system. The range of motions and the positional accuracy of this high precision stage in the *x*, *y*, and *z* directions were 100 μm ± 5 nm, 100 μm ± 5 nm, and 20 μm ± 2 nm, respectively. As mentioned earlier, only the *x* and *y* directions of this stage were enabled to achieve the relative motions between the sample and the tip. Thus, the stage displacement in the *z* direction was disabled. A diamond tip (PDNISP, Veeco Company, USA) was used for all nanomachining tests. The normal spring constant (K) of the cantilever, on which the tip is mounted, was 174 N/m as specified by the manufacturer. The radius of the diamond tip was approximately 85 nm. This was determined by the tip blind reconstruction method using a tip characterization specimen (RS-15M) (Dongmo et al., 2000).

The workpiece used in this study was a single crystal copper sample with (110) crystallographic plane (Hefei Ke Jing Materials Technology Co., Hefei, China). The scratching and the feed motions were in the [110] and [010] directions, respectively. This sample was polished by the manufacturer. The arithmetic mean roughness (Ra), estimated with tapping mode AFM measurements, was less than 5 nm. The radius of

the diamond tip was assumed to stay constant during all scratching tests because it is expected that negligible tip wear occurred when cutting the soft copper sample (Bowden and Tabor, 1950). After machining, a silicon nitride tip, with a normal spring constant of 0.35 N/m, was used to obtain the surface topography information of the produced nanostructures. Before this imaging step, the machined samples were ultrasonically cleaned in alcohol solution for about 10 min to remove the chips formed during machining.

2.2 Methodology

In previous studies, the authors investigated the dependence from the normal load (F_N) applied by the tip on the sample and the feed (f) of the scratching path on the resulting depth (h) of a machined nanochannel (Geng et al., 2013b). We found that both an increase of the normal load and a decrease of the feed lead to increasing the machined depth. Due to these inter-related effects, it is perhaps not surprising that most scholars implemented the more intuitive method whereby the normal load applied on the sample is varied while the feed remains constant during machining to achieve 3D-MNS (Geng et al., 2013b). However, as discussed in the Introduction section, this approach can result in a relatively time-consuming process to implement in practice due to the increased synchronization complexity between the stage lateral motions and the pre-defined tip vertical displacements. For this reason, we propose a novel AFM-based nanomachining method in this paper, which relies on the control of the distance between adjacent and parallel paths, as shown in Fig. 1 (a), while keeping

the normal load constant to determine the machined depth. This approach may be thought of as a feed-controlled method (illustrated in Figs. 1 (b) and (c)) as opposed to the more conventional normal force-controlled strategy. In Fig. 1 (b), the dotted line represents the theoretical cross section of a 3D-MNS machined by the AFM tip in this way. In particular, the two different tip positions, A and B, shown correspond to the deepest and the shallowest points of the nanostructure, respectively. *V* represents the AFM feed direction. Thus, to fabricate 3D-MNS, the high precision precision stage needs to move with different feed values along the *y* direction based on the pre-determined design of the 3D-MNS. Fig. 1 (c) illustrates the relation between different feed values that should be implemented along the cross section of the 3D-MNS represented in Fig. 1 (b). In this schematic, the feed values at points A and B are f_1 and f_2, respectively, where f_1 is smaller than f_2. Correspondingly, the cutting depth at point A is larger than that at point B (see Fig. 1 (b)). To guarantee the machining quality, edge-forward feed direction is selected in this study, in which the movement of the high-precision stage is parallel and towards the probe cantilever (Geng et al., 2016b).

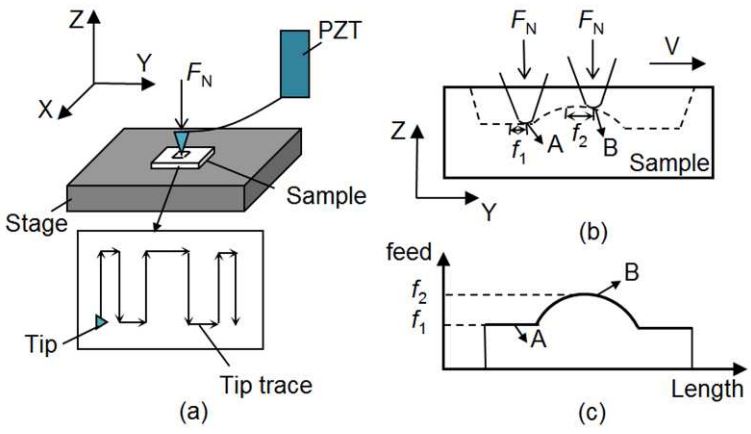

Fig. 1 (a) Schematic illustrating the 3D AFM-based mechanical machining process via the control of the scratching trajectory. (b) The dotted line denotes a 3D-MNS machined by the AFM tip. The feeds at points A and B are f_1 and f_2. (c) Feed control signal variation during the machining process of the 3D-MNS shown in Fig. 1 (b).

The detailed realization of a machining operation is described as follows. First, the AFM tip is approached towards the sample surface until the normal load applied by the tip on the material reaches a desired value, which is set beforehand by the user. This corresponds to the target value, which will subsequently be kept constant by the feedback loop of the AFM instrument during machining. Next, the cross section of the desired 3D-MNS is used to determine the machined depth profile which should be achieved along the feed direction. Corresponding feed values should then be evaluated based on the relation between the machined depth and the feed for a given normal load. This can be established experimentally by machining a number of square cavities with different feed values first and then by fitting a regression line to the plot of the machined depths as a function of the feed. The sum of the feed values is used to control the length of a given 3D-MNS. The scratching paths are perpendicular to the feed direction and the scratching speed is kept constant during the whole machining process. The width of a 3D-MNS is determined by the adopted length of the scratching paths, which was set to 20 μm in this study.

3. Results and discussion

3.1 Relationship between the feed and the machined depth

As mentioned above, the relationship between the machined depth and the feed should be established first. In a previous study, the authors proposed a model to express this dependence (Geng et al., 2013b). In this case, knowledge of the yield stress of the processed material is required. However, due to the difference in yield stress values when scratching in different crystallographic directions for single crystal materials, this model is not applied here. Although nanoindentation has been used in previous work to assess the yield stress (Geng et al., 2013b), this method may not be applicable to determine accurately the yield stress in the scratching direction, which is parallel to the sample surface (i.e. [110] in this study). For this reason, the evolution of the machined depth as a function of the feed was determined experimentally in this study. This was achieved by machining square cavities corresponding to different combinations of applied normal load and feed values. In particular, two different normal loads were considered, namely, 104.2 μN and 145.1 μN. These values were selected based on the results of a former study to guarantee the quality of the machined surface and to minimize the error associated the resulting depth (Geng et al., 2016a). In addition, eleven feed values were considered in the range 30 nm to 130 nm. Thus, twenty-two different square cavities were processed. The machined depth of each cavity was estimated as the average measurement at three different locations within the cavity. The results obtained are shown in Fig. 2. For each normal load, the data were then fitted to a quadratic function to express the relationship between the machined depth and the feed. The fitted functions are given by Eqs. (1) and (2). From

Fig. 2, it can be observed that the machined depth decreases when the feed increases and that a larger depth can be obtained using a relatively large normal load (145.1 μN).

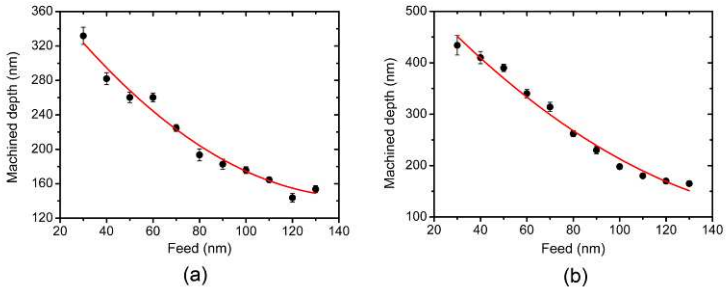

Fig.2 Relationship between machined depth and feed for different normal loads: (a) 102.4 μN and (b) 145.1 μN

$$h(f)_1 = 0.01391 f^2 - 3.99021 f + 431.996 \quad (1)$$

$$h(f)_2 = 0.0139 f^2 - 3.9902 f + 431.96 \quad (2)$$

3.2 Theoretical model of the machining process

In order to better understand the machining outcomes of the proposed method, a theoretical model is developed in this section. Based on the results of our previous studies (Geng et al., 2013b), the AFM probe-based nanomachining process can be considered as a hard abrasive particle scratching over a relatively soft substrate. As proposed by Bowden and Tabor (1950), in the plastic regime, the normal load applied on the sample surface (F_N) is equal to the yield stress (σ_p) of the sample material multiplied by the area (A_T) of the interface between the AFM probe and the sample,

projected horizontally. This is expressed in Eq. (3) below.

$$F_N = \sigma_p \cdot A_T \tag{3}$$

In this equation, A_T is a function of the machined depth (h) and the feed (f). In this study, the normal load is kept constant during the entire scratching process. Given that σ_p is considered a fixed material property, this means that A_T should also remain constant during the process. Thus, Eq. (3) holds true when the relationship between h and f leads to a constant A_T. Thus, the objective of the model proposed here is to express analytically the area A_T as a function of the feed and the depth for a given scratching path. The modelling approach adopted is based on that reported by Geng et al., (2013b). However, the proposed model extends the previous approach, which takes into account the change in feed and depth between two adjacent paths. The 3D schematic view of the machining process is shown in Fig. 3 (a). In Figs. 3 (b) and (c), the horizontal cross section of the tip is represented as a circle. This is due to the fact that it was verified by Geng et al. (2013b) that the AFM probe can be suitably described as a cone with a spherical apex when modelling the process. Thus, in this study, the shape of the AFM probe is also regarded as a cone with a spherical apex. The proposed method for fabricating 3D-MNS relies on varying the feed. Thus, the machining process can be divided in two scenarios, namely increasing feed and decreasing feed. In the first case, the current scratching path results in a smaller machined depth compared to the previous path. In the second case (i.e. decreasing feed), the obtained depth for the current path is larger than that machined during the previous scratching path. The detailed modelling process for each scenario is now described below.

(1) When the feed is increasing, the top view of the machining process is shown

in Fig. 3 (b). As shown in Fig. 3, the distance between the deepest points belonging to two adjacent paths is defined as the feed (f), which also represents the distance between two parallel machining lines. Also, these points are the respective centers of the horizontal circular cross sections of the AFM tip at the sample surface (denoted as the red and green dashed circles in Fig. 3) for each of these adjacent paths. In this figure, the edges of the previous and current paths are denoted by the numbers '1' and '2', respectively. The area of interest, A_T, which is the area of the interface between the tip and the sample projected horizontally is bounded by the blue solid line in this figure (i.e. region OCE). The point 'O' is the intersection point between two adjacent profiles when considering these profiles to be taken from a plane perpendicular to the scratching direction and through the axis of the probe. As represented in Fig. 3 (b), it is assumed that 'A' is an arbitrary point on the projected curve 'OC'. More specifically, 'OC' is the projection of the contact line between the tip (when scratching the current path) and the sample surface resulting from the previous path. Point 'B' is defined as the projection of point 'A' on the horizontal axis of the tip cross-section, i.e. on the line 'OE'. As detailed in (Geng et al., 2013b), the length L of the segment 'AB' is given by Eq. (4).

$$L = \sqrt{R_2^{\,2} - (R_1 - f)^2} \tag{4}$$

where R_1 and R_2 are the radii of the horizontal cross-sections of the AFM probe at a depth corresponding to 'A' for the previous and the current path, respectively. Given that the AFM probe is assumed to be a cone with a spherical apex, we need to consider whether the machined depth along a scratching path is larger than the height of the tip at which the transition between a spherical geometry to a conical one occurs. The height of this transition point is referred to as h_c. The depth difference between two adjacent paths is denoted Δh. The actual machined depth for the current path at

point A is represented by h. Thus, the expressions for R_1 and R_2 can be divided into three cases as follows depending on the value of h considered:

- When $0 < h+\Delta h < h_c$, the contact are between the tip and the material only occurs on the spherical apex of the tip. Thus, R_1 and R_2 can be expressed as:

$$\begin{cases} R_1 = \sqrt{r^2 - (r^2 - (h+\Delta h)^2)} \\ R_2 = \sqrt{r^2 - (r^2 - (h)^2)} \end{cases} \tag{5}$$

where r is the radius of the spherical apex. In this case, Δh always corresponds to a reduction in machined depth for the current path (in comparison with the previous path). If the semiangle of the cone the AFM probe is denoted α, then h_c is given by:

$$h_c = r(1-\sin\alpha) \tag{6}$$

- When $h_c < h+\Delta h$ and $0 < h < h_c$, this means that the contact area for previous path was on the conical part of the tip while that for the current path is only on the spherical apex. In this case, R_1 and R_2 can be obtained as follows:

$$\begin{cases} R_1 = r\cos\alpha + (h+\Delta h - (r - r\sin\alpha))\tan\alpha \\ R_2 = \sqrt{r^2 - (r^2 - (h)^2)} \end{cases} \tag{7}$$

- Finally, when $h_c < h$, the contact area involves the tip conical surface for both adjacent paths. Therefore, R_1 and R_2 can be calculated as:

$$\begin{cases} R_1 = r\cos\alpha + (h+\Delta h - (r - r\sin\alpha))\tan\alpha \\ R_2 = r\cos\alpha + (h - (r - r\sin\alpha))\tan\alpha \end{cases} \tag{8}$$

The variable x is defined as the length of the segment 'OB'. The position of point 'O' is between the two centers of the circular cross sections belonging to the former

and current paths as shown in Fig. 4 (a) and is dependent on the feed (*f*) and the machined depth. The height of point 'O' with respect to the depth of the current path is denoted (h_r) as shown in Fig. 4. Due to the very small feed values usually employed in comparison with the size of the tip, it is assumed h_r is always smaller than h_c. Thus, h_r can be obtained from Eq. 9.

$$\sqrt{r^2-(r-h_r)^2}+\sqrt{r^2-(r-(h_r+\Delta h)^2}=f \tag{9}$$

Based on Eq. (9), it can be said that point 'O' is closer to the center of the horizontal cross-section of the probe for the current path. In addition, using geometric relationships, it can be inferred that the lowest possible value for *x* is zero when point 'B*'* is coincident with point 'O' and that its highest possible value is when point 'B*'* is coincident with point 'D'. In this case, *x* is equal to $R_1'-\sqrt{r^2-(r-(h_r+\Delta h))^2}$ where R_1' is the radius of the horizontal cross-section of the probe at the sample surface for the previous path. Generally, *x* is expressed as follows:

$$x=R_1-\sqrt{r^2-(r-(h_r+\Delta h))^2} \tag{10}$$

Based on the different values of *L* which correspond to different depth values for point 'A', the area OCD can be obtained by integrating *L* with respect to *x*, as expressed by the following equation:

$$S_{OCD}=\int_0^{\sqrt{r^2-(r^2-(h_c)^2)}-\sqrt{r^2-(r-(h_r+\Delta h))^2}} Ldx+\int_{\sqrt{r^2-(r^2-(h_c)^2)}-\sqrt{r^2-(r-(h_r+\Delta h))^2}}^{(r\cos\alpha+(h_c+\Delta h-(r-r\sin\alpha))\tan\alpha)-\sqrt{r^2-(r-(h_r+\Delta h))^2}} Ldx+$$
$$\int_{(r\cos\alpha+(h_c+\Delta h-(r-r\sin\alpha))\tan\alpha)-\sqrt{r^2-(r-(h_r+\Delta h))^2}}^{R_1'-\sqrt{r^2-(r-(h_r+\Delta h))^2}} Ldx \tag{11}$$

The area CDE can be obtained by

$$S_{CDE}=\frac{1}{2}\arccos\left(\frac{R_1'-f}{R_2'}\right)\times R_2'^2-\frac{1}{2}(R_1'-f)\sqrt{R_2'^2-(R_1'-f)^2} \tag{12}$$

where R_2' is the radius of the horizontal cross-section of the probe at the sample surface for the current path. R_1' and R_2' can be expressed by

$$\begin{cases} R_1' = r\cos\alpha + (h_t + \Delta h - (r - r\sin\alpha))\tan\alpha \\ R_2' = r\cos\alpha + (h_t - (r - r\sin\alpha))\tan\alpha \end{cases} \tag{13}$$

where h_t is the machined depth of the groove for the current machining path from the sample surface. Therefore, the horizontal projected area A_T can be described by

$$A_T = S_{OCD} + S_{CDE} \tag{14}$$

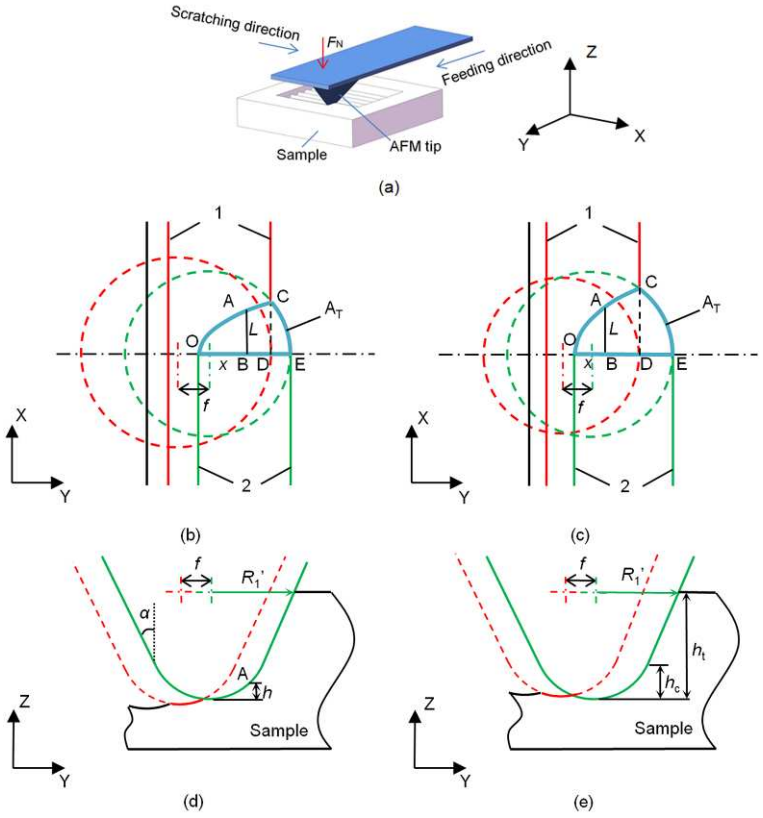

Fig. 3 (a) Schematic view of the motion of the AFM tip during the scratching process. (b) and (c) Top views of the machining process when the feed is increasing, (b) and when the feed is decreasing, (c). (d) and (e) Front views of the machining process when the feed is increasing, (d) and when the feed is decreasing, (e).

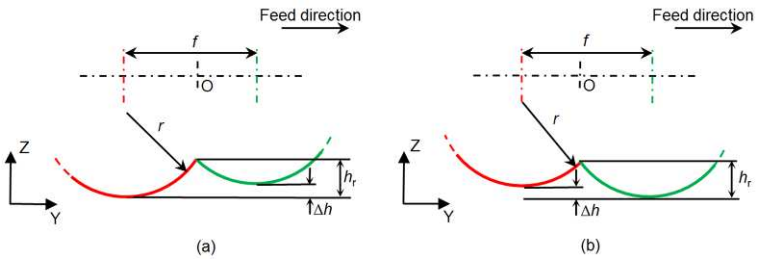

Fig. 4 Side views of the 3D-MNS fabrication process. Feed increasing, (a) and feed decreasing, (b).

(2) When the feed is decreasing, the top view of the machining process is shown in Fig. 3 (c). In comparison with the previous "feed increasing" scenario, the radius of the horizontal cross-section of the AFM probe at the sample surface for the current path is larger than that for the previous path. In this case, the length (L) of the segment 'AB' can also be obtained from Eq. (4). In addition we should consider that reducing the feed leads to the machined depth of the current path becoming larger than that from the previous path. For this reason, the sign of Δh, the depth difference between two adjacent paths, should be changed. As a result, the expressions for R_1 and R_2 are now given by Eqs. (15), (16) and (17) below, based on the considered height for point 'A'.

- When $0 < h < h_c$, R_1 and R_2 can be expressed as follows:

$$\begin{cases} R_1 = \sqrt{r^2 - (r^2 - (h\text{-}\Delta h)^2)} \\ R_2 = \sqrt{r^2 - (r^2 - (h)^2)} \end{cases} \tag{15}$$

- When $h_c < h$ and $0 < h\text{-}\Delta h < h_c$, then R_1 and R_2 are given by:

$$\begin{cases} R_1 = r\cos\alpha + (h - \Delta h - (r - r\sin\alpha))\tan\alpha \\ R_2 = \sqrt{r^2 - (r^2 - (h)^2)} \end{cases} \tag{16}$$

- Finally, when $h_c < h-\Delta h$, R_1 and R_2 are expressed:

$$\begin{cases} R_1 = r\cos\alpha + (h - \Delta h - (r - r\sin\alpha))\tan\alpha \\ R_2 = r\cos\alpha + (h - (r - r\sin\alpha))\tan\alpha \end{cases} \tag{17}$$

The relationship between h_r and f is now given by

$$\sqrt{r^2 - (r - h_r)^2} + \sqrt{r^2 - (r - (h_r - \Delta h)^2} = f \tag{18}$$

The range of possible values for x is now comprised between zero and $R_1' - \sqrt{r^2 - (r - (h_r - \Delta h))^2}$. In particular, x is given by

$$x = R_1 - \sqrt{r^2 - (r - (h_r - \Delta h))^2} \tag{19}$$

It should also be noted that, the position of point 'O' is different from that defined earlier for the feed increase scenario. More specifically, point 'O' is now closer to the center of the circular horizontal cross-section of the probe for the previous path as shown in Fig. 4 (b). Finally, the area OCD is now given by:

$$S_{OCD} = \int_0^{\sqrt{r^2-(r^2-(h_c-\Delta h)^2)}-\sqrt{r^2-(r-(h_r-\Delta h))^2}} L dx + \int_{\sqrt{r^2-(r^2-(h_c-\Delta h)^2)}-\sqrt{r^2-(r-(h_r-\Delta h))^2}}^{(r\cos\alpha+(h_c-(r-r\sin\alpha))\tan\alpha)-\sqrt{r^2-(r-(h_r-\Delta h))^2}} L dx + \int_{(r\cos\alpha+(h_c-(r-r\sin\alpha))\tan\alpha)-\sqrt{r^2-(r-(h_r-\Delta h))^2}}^{R_1'-\sqrt{r^2-(r-(h_r-\Delta h))^2}} L dx \tag{20}$$

The formula used to express the area of the region CDE is the same as that already defined for the previous scenario. Thus, it is given by Eq. (12). However, the expressions for R_1' and R_2' are now changed to:

$$\begin{cases} R_1' = r\cos\alpha + (h_t - \Delta h - (r - r\sin\alpha))\tan\alpha \\ R_2' = r\cos\alpha + (h_t - (r - r\sin\alpha))\tan\alpha \end{cases} \quad (21)$$

Thus, the area (A_T) can also be calculated by summing S_{OCD} and S_{CDE}.

3.3 Critical value of the slope of the nanostructures

When conducting the AFM tip-based mechanical machining process, the inclination angle of the tip surface results the generation of a slope on the side of a machined nanogroove. For this reason, a surface slope for fabricated nanostructures is always present in the feed direction. This is one of the reasons why it is difficult to form nanostructures with a steep slope using this process. Moreover, in this study, the change in feed values between two adjacent scratching paths represents a different configuration from the case where cavities are machined with a constant feed. This can introduce machining errors for the slope of the fabricated nanostructures. More specifically, the larger the difference between two consecutive feed values, that is, the larger the desired slope of the nanostructure, the more prominent the machining error is expected. This phenomenon can be verified experimentally as presented in details later on in this section.

In order to use the fabrication method described in the previous section 2.2, the consecutive feed values for the entire machining process should be obtained first. Fig. 5 summarizes the algorithm employed to determine such feed values and thus, the probe trajectory along the length of a 3D-MNS. To start with, the relationship $h=g(f)$

that defines the machined depth as a function of the feed should be determined for a given normal load. This can be achieved experimentally as shown in section 3.1. In addition, the mathematical expression $h=k(d)$ describing the profile of the designed 3D-MNS along its length should also be determined. In this notation, d represents the distance along the profile from the initial scratching position. Based on an initial machined groove at a depth (h_1), the feed for the subsequent scratching path (f_1) can be calculated using $h=g(f)$. The position of the second path (d_2) can then be easily derived by d_1+f_1. Next, the desired machined depth (h_2) for the second path is obtained from $h=k(d)$ based on the value of d_2. Similarly to the previous step, applying $h=g(f)$, the feed for the next scratching path (f_2) can be calculated, and so on. After i-1 iterations, based on the obtained f_{i-1}, the machining position for the i^{th} scratching path (d_i) can be derived by $d_{i-1}+f_{i-1}$. Then, d_i is compared with the expected length of the nanostructure ($d_{expected}$). If $d_i \geq d_{expected}$, the machining process is completed. Otherwise, the machining cycle is continued until the distance from the initial machining position is larger than $d_{expected}$.

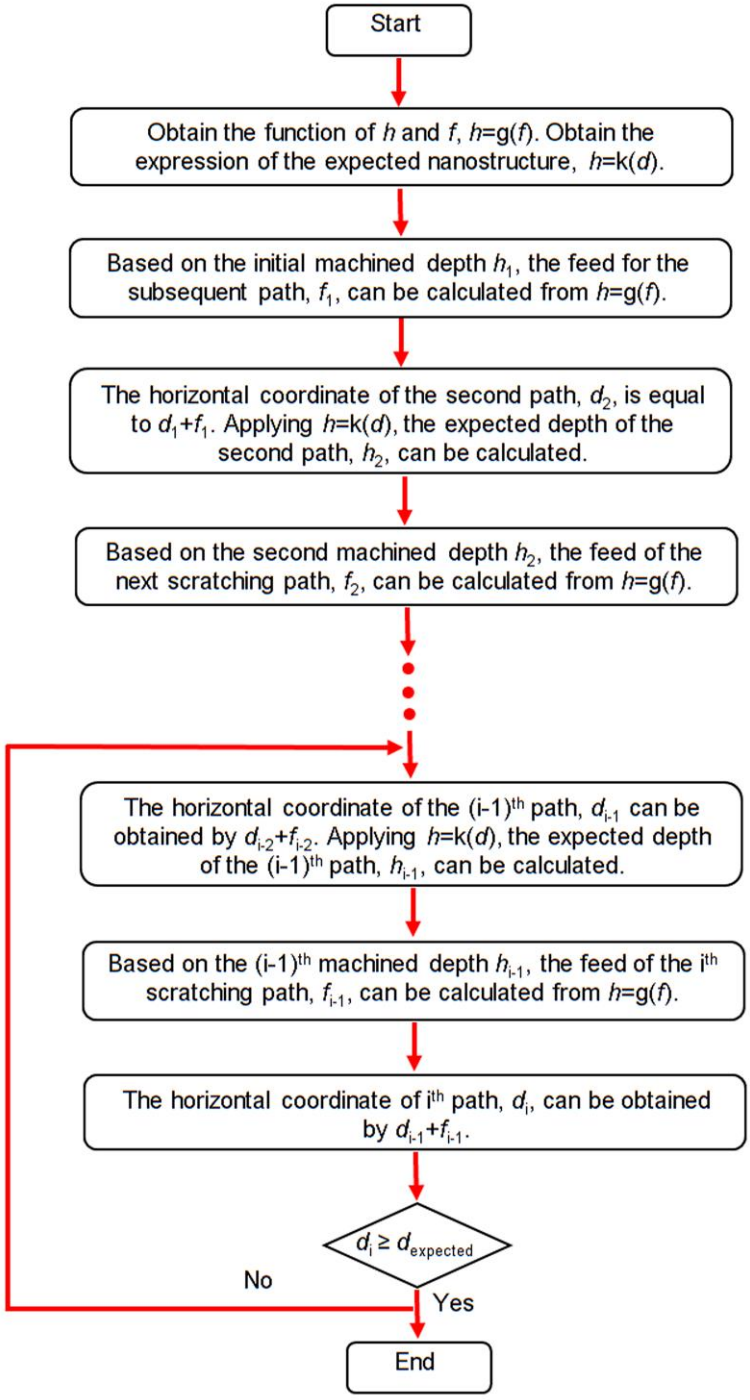

Fig. 5 Algorithm used to define the feed values to be applied along the length of a 3D-MNS.

Both cases of feed increasing and feed decreasing are now evaluated. Fig. 6 (a) shows desired profiles for nanostructures with negative (-12°) and positive slope

(+12°), respectively. In this example, the depths of the top and bottom surfaces are 125 nm and 400 nm, respectively. Thus, the amplitude of this structure is 275 nm. For the calculation, the normal load is chosen as 145.1 μN and thus Eq. (2) is considered. Based on the algorithm described above, the corresponding feed values for each scratching path are obtained, as shown in Fig. 6 (b). From Fig. 6 (b), it can be observed that the evolution of the feed is nonlinear with the number of scratching paths. In addition, it should be noticed that the number of required scratching paths increases when processing with a relatively small feed (i.e. when the desired machined depth increases) to achieve a constant slope.

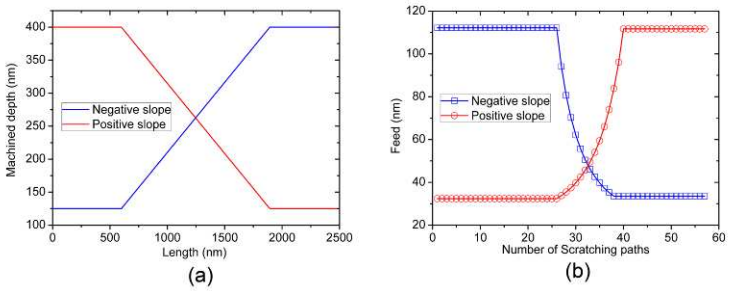

Fig. 6 (a) Designed cross sectional profile of nanostructures and (b) obtained corresponding feed values.

Figs. 7 (a) and (b) show the AFM images of the fabricated nanostructures with the expected slope of -12° and +12°, respectively. These were machined using the obtained feed values in Fig. 6 (b). From these data, it could be verified that the machined depths of these nanostructures were very close to the expected values. In addition, the region on the profile cross-section where the designed slope is located

was used to conduct a linear fitting on the profile data. This was achieved to calculate the value of the slope obtained experimentally. In this way, the experimental slope values were measured to be -12.04° and 11.49°, respectively. Thus, they are very close to the expected values. Larger values of the slope were also studied, namely -30° and +30°, to evaluate the maximum achievable slope, i.e. the critical slope. Fig. 8 shows the AFM images of the fabricated nanostructures in this case. The designed depths for the top and bottom surface were the same as those in the previous experiment. In addition, the normal load was also chosen to be 145.1 μN. It can be observed from this figure that the machined depths for the achieved nanostructures were also close to the expected values. However, the slopes of these nanostructures were measured to -16.60° and 14.36°, respectively, which are much lower than the expected values of -30° and +30°. The possible reason for this discrepancy can be explained as follows. First, as shown in Figs. 3 (b) and (c), in order to guarantee the machining precision, adjacent scratching paths should not affect each other during the machining process, that is, R_1' should be less than R_2'+f in the feed increasing condition and R_2' should less R_1'+f in the feed decreasing case. Appling Eqs. (13) and (21), an inequation can be derived for these two cases, as follows.

$$\frac{\Delta h}{f} < \tan(\frac{\pi}{2} - \alpha) \tag{22}$$

The ratio of Δh and f represents the slope of the nanostructure. In this study, the semiangle (α) of the cone the AFM probe utilised is assumed to be 60° based on SEM measurements. Based on Eq. (22), it was found that the slope of the expected nanostructure should be less than 30°.

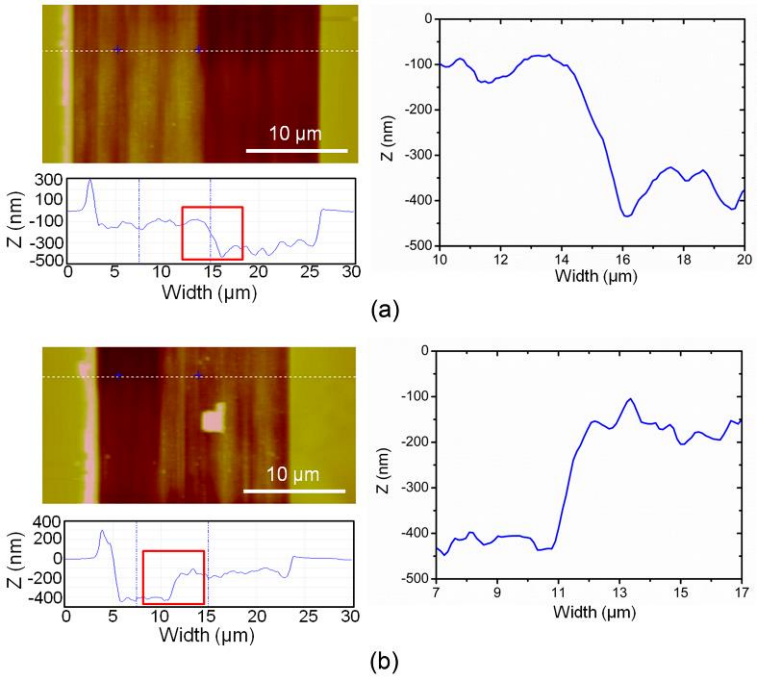

Fig. 7 AFM images of machined nanostructures, which exhibit a desired slope of (a) -12˚ and (b) 12˚ on the floor surface.

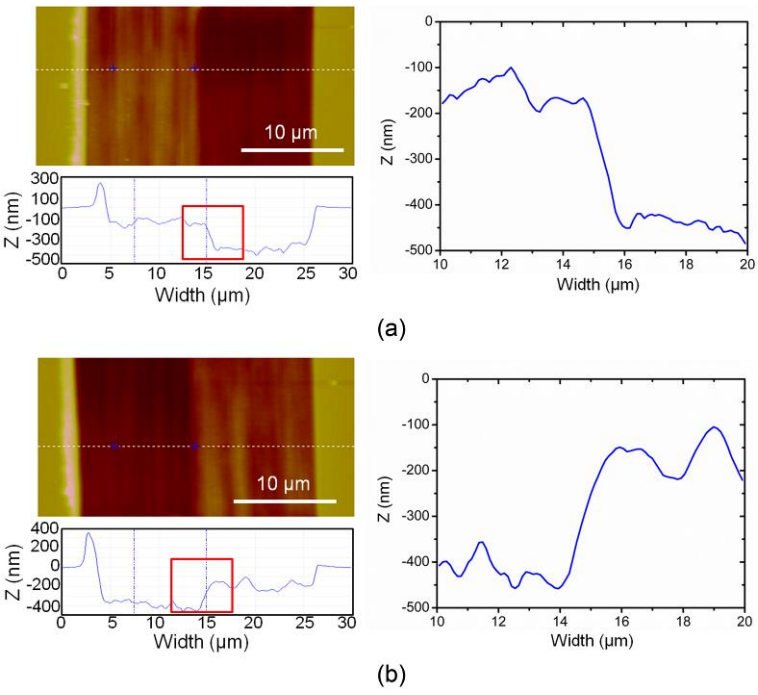

Fig. 8 AFM images of obtained machined nanostructures for a targeted slope of (a)

-30˚ and (b) 30˚ on the floor surface.

In addition, when machining cavities with planar floor surface using the constant feed method as reported in our previous study (Geng et al., 2013b), point 'O' in Figs. 3 (b) and (c) should be in the middle of the two centers of the red and green dashed circles. However, from Eqs. (9) and (18), it can be observed that point 'O' is closer to the center of the cross-section of the probe for the latter path with an increasing feed, while it is closer to the center of the cross-section of the probe in the previous path in the case of feed decreasing. According to Eqs. (10) and (19), although, the range of values that the variable x can take may be larger in the case of feed increasing and smaller in the condition of feed decreasing compared with those for flat floor cavities, the total length (OE) used to calculate the area A_T is smaller in the situation of feed increasing and larger in the case of feed decreasing. Moreover, it can be indicated easily from Eq. (4) that L is smaller in the condition of feed increasing and larger in the case of feed decreasing compared with the case of machining cavities with flat floor, in which R_1' equals R_2'. Thus, from Eq. (14), the sum of S_{OCD} and S_{CDE}, that is, the horizontal projected area representing the interaction between the AFM probe and the sample surface (A_T) becomes smaller when the feed is increasing and larger in the condition of feed decreasing. Fig. 9 shows schematic diagrams of the machining processes for flat floor cavities and for nanostructures with positive and negative slopes, respectively. In this figure, the red line represents the contact length between the AFM probe and the sample surface. It can be observed that, for a given machined

depth for the second path, h_2, and a given feed for the second feed, f_2, the contact length is the smallest for the case of feed increasing (Fig. 9 (b)) and the largest for the condition of feed decreasing (Fig. 9 (c)). The same conclusion could be made for A_T. Based on the relationship, found a-priori from the machining of cavities with flat floors, to express the evolution of the feed as a function of the machined depth, it is can be said that for a pre-set normal load F_N, the probe should penetrate into the sample surface deeper when scratching with a feed higher than that of the previous path. This enlarges the contact area between the probe and the sample surface. This is a result of the feedback loop mechanism implemented in AFM instruments to balance the applied normal load. Thus, in practice, the machined depth for the second path should be larger than the excepted value in this case. This can lead to a reduction of the slope of the nanostructure. Similarly, for the feed decreasing case, the penetration depth of the probe into the sample surface should be lower when scratching with a larger feed. This is because the contact area between the AFM probe and the sample surface should be reduced to balance the normal load. Thus, the machined depth should be less than the expected value, which can also lead to a reduction of the slope of the nanostructure. Moreover, it can be indicated that the reduction of the slope can be intensified by enlarging the difference between feed values of adjacent scratching path. By using the relationship between the feed and the machined depth to fabricate 3D-MNS based on the proposed method, the achieved slope of the nanostructure should be, to some extent, less than that of the designed value.

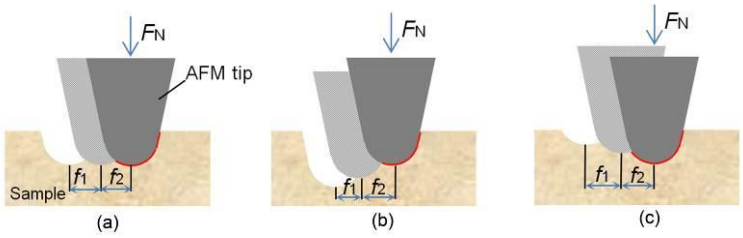

Fig. 9 Schematic of the contact length between the tip and the sample for the machining process of surfaces with different inclined angles (a) flat floor surface, (b) positive slope and (c) negative slope.

Therefore, a series of experiments were conducted to study the range of slope values achievable in practice. This was achieved for two different normal loads, namely 102.4 μN and 145.1 μN, and for desired slopes comprised between -30° and -8° and also between +8° and +30°. For each normal load, 15 nanoscratching tests were conducted to study the achievable slope using the proposed method. After the machining process, the errors (n_{error}) between the obtained and desired slope values of the nanostructures were calculated using Eq. (23).

$$n_{error} = \frac{D_e - D_r}{D_r} \tag{23}$$

where D_e and D_r are the experimental and the expected values of the slope, respectively. Fig. 10 displays the plots of the machining errors as a function of the desired slope value. It can be observed from this figure that n_{error} is almost consistent for the different applied normal loads and that slope values comprised between -12° and +12° should be selected to guarantee a machining error within 10%. Moreover, as reported in this figure, the machining errors are mainly negative. This shows that the

experimental values of the slope are less than the expected ones. This result reinforces the points made in the discussion above.

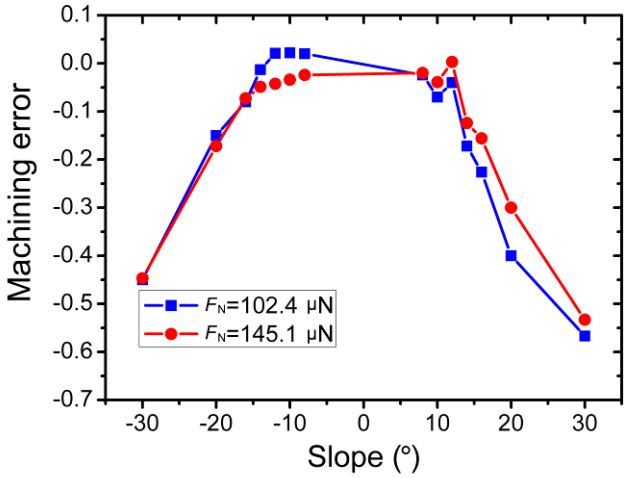

Fig. 10 Machining errors when fabricating inclined surfaces with different normal loads

3.4 Demonstration of 3D-MNS fabricated by the proposed method

In this study, typical sinusoidal waveforms nanostructures were selected to demonstrate the feasibility of the proposed method. Due to the design constraint associated with the critical slope for 3D-MNS fabricated in this way, the amplitude and period of desired nanostructures should be considered carefully. It can be assumed that the expected sinusoidal profile for a 3D-MNS can be expressed according to Eq. (24).

$$f(d) = b - a\sin(\omega d) \tag{24}$$

where a and b are the amplitude and the base depth of the desired sinusoidal waveforms nanostructure.

Thus, the maximum value of the slope can be obtained as $-a\omega$. Based on the discussion in the above section, this maximum value should be less than $\tan(\theta_c)$ where θ_c is the critical value of the slope. Thus, the period of the expected sinusoidal waveforms nanostructure (T) should satisfy the inequation in Eq. (25) below.

$$T \geq \frac{2\pi a}{\tan(\theta_c)} \tag{25}$$

From this, it can be said that, when the designed amplitude is selected as 80 nm, the period should be chosen as a value larger than or equal to 2.4 μm. For this reason, we chose the period to be 2.4 μm. In addition, the base depth was chosen as 240 nm and thus, the normal load could be selected as 102.4 μN. Based on these values, the theoretical profile of the cross section of the 3D-MNS can be calculated as reported with Eq. (26). Fig. 11 (a) shows 2D and 3D AFM images of the corresponding fabricated nanostructure. From the analysis of the measured cross-section, it can be observed that the base depth is around 250 nm and the amplitude is about 70 nm to 80 nm, which are both in close agreement with the expected values. The maximum machining error for the achieved depth is around 20 nm to 30 nm, which is less than 10% of the total desired machined depth. This result is considered acceptable in the context of nanomechanical machining. In addition, the period of this machined nanostructure is measured to be about 2.4 μm, which is again consistent with the predefined value. This indicates that the designed value for the period can be easily

achieved in an accurate manner using the method proposed in this research. It should be noted that this result is also better than that achieved with an alternative method reported in our previous study (Geng et al., 2016a), which relies on controlling the frequency of the tip reciprocating motions. An additional experiment was conducted for the normal load of 145.1 μN. In this case, the base depth and the amplitude were selected as 275 nm and 125 nm, respectively. Applying Eq. (25), the minimum value of the period of the sinusoidal waveforms was calculated as 3.74 μm. Thus, the period was chosen as 4 μm. The corresponding expression of the expected sinusoidal waveforms profile is given by Eq. (27). Fig. 11 (b) shows 2D and 3D AFM images of the machined sinusoidal waveforms nanostructure. From Fig. 11 (b), it can be observed that the base depth is around 270 nm and that the amplitude is essentially comprised in the range from 115 nm to 125 nm. Moreover, the period of the nanostructure was measured as 4 μm. These results are consistent with the expected values. This further demonstrates the feasibility and suitability of the presented nanomechanical machining method to fabricate 3D-MNS.

$$f(d) = 240 - 80\sin(0.00243d) \tag{26}$$

$$f(d) = 275 - 125\sin(0.00156d) \tag{27}$$

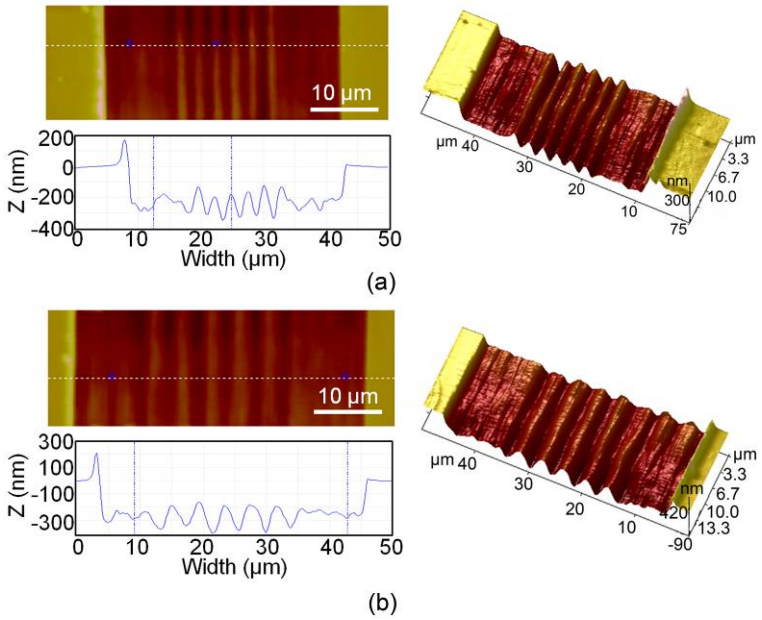

Fig. 11 AFM images of the machined nanochannels with desired sinusoidal waveforms nanostructures on the floor surface: (a) the period of 2.4 μm and (b) the period of 4 μm.

In addition to 3D-MNS with sinusoidal profiles, half-triangle and top-hat waveforms nanostructures were also fabricated in this study. For the half-triangle waveforms, as expressed in Eq. (28), the normal load was 145.1 μN and the selected amplitude was 250 nm. The largest machined depth for this nanostructure was defined as 400 nm and the slope of both sides of the triangle were selected as +12° and -12°. In addition, the triangular part of the waveform accounted for 30% of the whole period while the remaining part was planar. Thus, the period of this nanostructure could be calculated to be 7.93 μm. Fig. 12 (a) shows the AFM image of the fabricated nanostructure for such a half-triangle waveform. It can be observed that the total machined depth was about 400 nm, which is consistent with the desired value.

However, the amplitude was around 210 nm, which is 16% less than the expected value. The possible reason can be explained as follows. As shown in Fig. 6 (b), a relatively small machined depth can be obtained by a relatively large feed and less machining paths are needed when scratching with a relatively large feed to achieve the same slope. Thus, the feed values used for fabricating this nanostructure were relatively large on the top of the triangular shape. In turn, the number of machining paths is relatively small when scratching in this region of the waveform. Thus, it is difficult to fabricate the apex of the triangular waveform by using a relatively large feed. Moreover, the AFM probe has a relative large radius, 85 nm in this study. This can also introduce a machining error for the apex of the triangular waveform. Therefore, is is expected that the amplitude of the half-triangle waveform is smaller than the designed value.

$$f(d)=\begin{cases}400-0.213d, & nT<d\le(n+0.15)T\\ 400+0.213d, & (n+0.15)T<d\le(n+0.3)T\\ 400, & (n+0.3)T<d\le(n+1)T\end{cases} \tag{28}$$

For the top-hat waveforms design, the amplitude was chosen as 200 nm and the total machined depth was defined as 400 nm. The bottom part of the waveform was designed to occupy half of the the profile for one period. The expression of the expected waveform is shown in Eq. (29). Fig. 12 (b) shows the AFM image of the corresponding fabricated 3D-MNS. From this data, it can be measured that the slope of the edge of the obtained profile is around 15°, which is much smaller than the

expected value of 90°. This result illustrates suitably the design constraint associated with the critical slope, as discussed earlier in this paper. Thus, this proposed method should not be employed for fabricating 3D-MNS with vertical walls.

$$f(d)=\begin{cases}400, & nT<d\le(n+0.5)T\\ 200, & (n+0.5)T<d\le(n+1)T\end{cases} \tag{29}$$

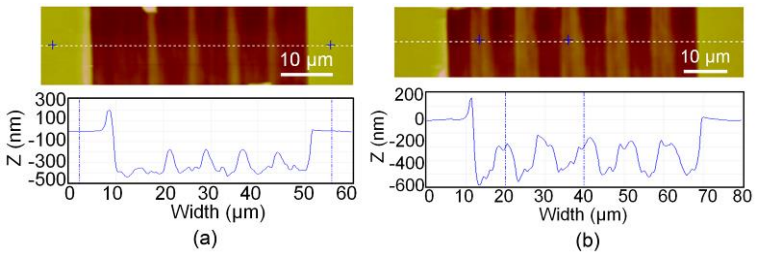

Fig. 12 Fabricated 3D-MNS for different waveform designs: (a) half-triangular profile and (b) top-hat profile.

4. Conclusions

This paper presented a novel AFM tip-based mechanical nanomachining approach to fabricate three-dimensional micro- and nanostructures (3D-MNS) according to pre-designed profiles which can be realized in the feed direction of the tip. This means that the method is suitable for fabricating 3D-MNS for which the topography does not change along their width but along their length. The machining of several types of periodic nanostructures was demonstrated on a single crystal copper workpiece. In addition, a machining model was presented to gain further understanding of the observed results. This model considered the relationship between

the feed and the machined depth as a function of the contact area between the tip and the material.

An important advantage of the proposed method is that it is based on the separation of 1) the vertical motions of the tip, which are controlled by the feedback loop of the AFM instrument to keep the normal applied load constant, and 2) the lateral displacements of the stage. As a result, this method has the potential to be applied directly on other AFM systems or on devices, which enable the control of the normal applied load such as nano-indenters. A drawback however, is that nanostructures with top-hat waveforms or with large slopes cannot be achieved using the proposed method. Based on the theoretical model developed in this study the slope of the expected nanostructure was determined to be less than 30°. This was further validated using experimental tests. In fact, these tests revealed that slope values comprised between -12° and +12° should be selected to guarantee a machining error within 10%.

Finally, it is worth mentioning that the total machining time for the two given sinusoidal waveforms nanostructures was around 10 min, which is dependent on the feed values selected in the machining process and the scratching speed used in this study (around 20 μm/s). The areal output per time was around 100 μm^2/min when the scratching speed was 20 μm/s and the feed selected was 80 nm. The maximum surface area that could be machined in this study was 100 μm × 100 μm. This area is

limited by the displacement range of the high precision stage used. This method can be applied to some soft metals, such as aluminum alloy, single crystal copper, gold or platinum thin film. However, for ferrous metal, a chemical reaction between carbon of the diamond and iron of the ferrous metals could take place depending on the process temperature and increases the tip wear significantly. Thus, this proposed method is not unsuitable for the machining of ferrous metals.

Acknowledgments

The authors gratefully acknowledge the financial supports of the Foundation for Innovative Research Groups of the National Natural Science Foundation of China (51521003), the National Natural Science Foundation of China (21327002), Self-Planned Task (SKLRS201606B) of State Key Laboratory of Robotics and System (HIT), the Program for New Century Excellent Talents in University (NCET-11-0812) and the National Program for Support of Top-notch Young Professors.

References

Binning, G., Quate, C. F., Gerber, C., 1986. Atomic force microscope. Phys. Rev. Lett. 56 (9), 930-933.

Bowden, F.P., Tabor, D., 1950. The friction and lubrication of solids. Oxford University Press, Oxford.

Chen, C. F., Tzeng, S. D., Chen, H. Y., Gwo, S., 2005. Silicon microlens structures fabricated by scanning-probe gray-scale oxidation. Opt. Lett. 30(6), 652-654.

Deng, J., Zhang, L., Dong, J., Cohen, P. H., 2016. AFM-based 3D nanofabrication using ultrasonic vibration assisted nanomachining. J. Manuf. Process. 24, 195-202.

Dongmo, L. S., Villarrubia, J. S., Jones, S. N., Renegar, T. B., Song, J. F., 2000. Experimental test of blind tip reconstruction for scanning probe microscopy. Ultramicroscopy 85, 141-153.

Garcia, R., Knoll, A. W., Riedo, E., 2014. Advanced scanning probe lithography. Nat. Nanotechnol. 9, 577-587.

Li, J. F., Huang, Y. F., Ding, Y., Yang, Z. L., Li, S. B., Zhou, X. S., Fan, F. R., Zhang, W., Zhou, Z. Y., Wu, D. Y., Ren, B., Wang, Z. L., Tian, Z. Q., 2010. Shell-isolated nanoparticle-enhanced Raman spectroscopy. Nature 464, 392-395.

Lyshevski, S. E., 2002. MEMS and NEMS: Systems, Device, and Structures. CRC press, Boca Raton, FL, pp. 18-24.

Geng, Y. Q., Yan, Y. D., Zhao, X. S., Hu, Z. J., Liang, Y. C., Sun, T., Dong, S., 2013a. Fabrication of millimetre scale nanochannels using the AFM tip-based nanomachining method. Appl. Surf. Sci. 266, 386-394.

Geng, Y., Yan, Y., Xing, Y., Zhao, X., Hu, Z., 2013b. Modelling and experimental study of machined depth in AFM-based milling of nanochannels. Int. J. Mach. Tool. Manuf. 73, 87-96.

Geng, Y., Yan, Y., Brousseau, E., Cui, X., Yu, B., Zhao, X., Hu, Z., 2016a. Machining complex three-dimensional nanostructures with an atomic force microscope through

the frequency control of the tip reciprocating motion. J. Manuf. Sci. Eng. 138, 124501.

Geng, Y., Yan, Y., Brousseau, E., Yu, B., Qu, S., Hu, Z., Zhao, X., 2016b. Processing outcomes of the AFM probe-based machining approach with different feed directions. Precis. Eng.-J. Int. Soc. Precis. Eng. Nanotechnol. 46, 288-300.

Guo, J., Yu, B., Chen L., Qian, L., 2015. Nanodestructive nanofabrication on Si (100) surface by tribochemistry induced selective etching. Sci. Rep. 5, 164472.

Thompson, S. E. and Parthasarathy, S., 2006. Moore's law: the future of Si microelectronic. Mater. Today 9, 20-25.

Pries, D., Hedrick, J. L., Silva, A. D., Frommer, J., Gotsmann, B., Wolf, H., Despont, M., Duerig, U., Knoll, A. W., 2010. Nanoscale three-dimensional patterning of molecular resists by scanning probes. Science 328, 732-735.

Tseng, A. A., 2011. Advancements and challenges in development of atomic force microscopy for nanofabricatin. Nano Today 6, 493-509.

Xu, Z. W., Fang, F. Z., Fu, Y. Q., Zhang, S. J., Han, T., Li, J. M., 2009. Fabrication of micro/nano-structures using foucused ion beam implantation and XeF_2 gas-assisted etching. J. Micromech. Microeng. 19(5), 054003.

Yao, J. M., Le, A. P., Schulmerich, M. V., Maria, J., Lee, T. W., Gray, S. K., Bhargava, R., Rogers, J. A., Nuzzo, R. G., 2011. Soft embossing of nanoscale optical and plasmonic structures in glass. ACS Nano 5 (7), 5763-5774.

Yan, Y., Geng, Y., Hu, Z., 2015. Recent advances in AFM tip-based nanomechanical machining. Int. J. Mach. Tool. Manuf. 99, 1-18.

Yan, Y., Geng, Y., Hu, Z., Zhao, X., Yu, B., Zhang, Q., 2014. Fabrication of nanochannels with ladder nanostructure at the bottom using AFM nanoscratching method. Nanoscale Res. Lett. 9, 212.

Yan, Y., Hu, Z., Zhao, X., Sun, T., Dong, S., 2010. Top-down nanomechanical machining of three-dimensional nanostructures by atomic force microscopy. Small 6 (6), 724-728.

Zhan, D. P., Han, L. H., Zhang, J., Shi, K., Zhou, J. Z., Tian, Z. W., Tian, Z. Q., 2016. Confined chemical etching for electrochemical machining with nanoscale accuracy. Accounts Chem. Res. 49(11), 2596-2604.

Figure captions

Fig. 1 (a) Schematic illustrating the 3D AFM-based mechanical machining process via the control of the scratching trajectory. (b) The dotted line denotes a 3D-MNS machined by the AFM tip. The feeds at points A and B are f_1 and f_2. (c) Feed control signal variation during the machining process of the 3D-MNS shown in Fig. 1 (b).

Fig.2 Relationship between machined depth and feed for different normal loads: (a) 102.4 μN and (b) 145.1 μN

Fig. 3 (a) Schematic view of the motion of the AFM tip during the scratching process. (b) and (c) Top views of the machining process when the feed is increasing, (b) and when the feed is decreasing, (c).

Fig. 4 Side views of the 3D-MNS fabrication process. Feed increasing, (a) and feed decreasing, (b).

Fig. 5 Algorithm used to define the feed values to be applied along the length of a 3D-MNS.

Fig. 6 (a) Designed cross sectional profile of nanostructures and (b) obtained corresponding feed values.

Fig. 7 AFM images of machined nanostructures, which exhibit a desired slope of (a) -12˚ and (b) 12˚ on the floor surface.

Fig. 8 AFM images of obtained machined nanostructures for a targeted slope of (a) -30˚ and (b) 30˚ on the floor surface.

Fig. 9 Schematic of the contact length between the tip and the sample for the machining process of surfaces with different inclined angles (a) flat floor surface, (b) positive slope and (c) negative slope.

Fig. 10 Machining errors when fabricating inclined surfaces with different normal loads

Fig. 11 AFM images of the machined nanochannels with desired sinusoidal waveforms nanostructures on the floor surface: (a) the period of 2.4 μm and (b) the period of 4 μm.

Fig. 12 Fabricated 3D-MNS for different waveform designs: (a) half-triangular profile and (b) top-hat profile.